Deep-tissue Imaging using Selective Plane Illumination Microscopy in *Drosophila*

Mayank Kumar

Supervisor:
Prof. Maria Leptin
EMBL

Advisor:
Dr. Chaitanya Athale
IISER PUNE

IISER PUNE

BS-MS Student
Indian Institute of Science Education and Research(IISER), Pune
2017-18

CERTIFICATE

This is to certify that this dissertation entitled **Deep-tissue Imaging using Selective Plane Illumination Microscopy in *Drosophila*** towards the partial fulfilment of the BS-MS dual degree programme at Indian Institute of Science Education and Research, Pune represents study/work carried out by **Mayank Kumar** at **European Molecular Biology Laboratory, Heidelberg** under the supervision of **Prof. Maria Leptin, Director, EMBO** during the academic year 2017-18.

Mayank Kumar

Mayank Kumar
IISER Pune

Prof. Maria Leptin
Director, EMBO

DECLARATION

I hereby declare that the matter embodied in the report entitled **Deep-tissue Imaging using Selective Plane Illumination Microscopy in *Drosophila*** are the results of the work carried out by me at the **European Molecular Biology Laboratory, Heidelberg**, under the supervision of **Prof. Maria Leptin** and the same has not been submitted elsewhere for any other degree.

Mayank Kumar

Mayank Kumar
IISER Pune

Prof. Maria Leptin
Director, EMBO

Abstract

The imaging speed and penetration depth limit the study of dynamics of the lateral mesodermal cells during gastrulation in Drosophila. Selective Plane Illumination Microscope (SPIM) is an important tool to image the rapid cell shape changes on the whole-organism level. However, both illumination light and fluorescence signal are strongly scattered in the fly embryos which reduces the contrast in images. To improve the deep-tissue imaging using SPIM, we developed new membrane markers with fluorophores that emit in the far-red and near-infrared region of electromagnetic spectrum. Also, we used deconvolution to improve the contrast in the acquired images by computationally reducing the noise and blur. Use of fluorophores emitting at longer wavelengths and deconvolution helps in producing more interpretable images with high signal-to-noise ratio at greater depths. Such images will facilitate the image analysis and thus generate a reliable 3D reconstructions of cells which will be essential in quantitative analyses of shape changes in the lateral mesodermal cells.

Contents

Abstract ii

Introduction **1**

1.1 Fluorescence Microscopy 1

1.1.1 Challenges in fluorescence microscopy 3

1.2 Selective Plane Illumination Microscopy 4

1.3 Deconvolution in Optical Microscopy 6

1.4 Ventral furrow formation in *Drosophila melanogaster* 7

Materials and Methods **11**

2.1 Methodology 11

2.2 Generation of transgenic fly stocks 12

2.2.1 Plasmid Construction 13

2.2.2 Fly transformation and Stock generation 14

2.3 Fly stocks 15

2.4 Imaging Protocol 16

2.4.1 Sample Preparation 16

2.4.2 SPIM Imaging 16

2.4.3 Image Processing 17

Results **19**

3.1 Comparison of different fluorophores as membrane markers 19

3.2 Computationally restoring noise and blur using deconvolution 21

Discussion **24**

Bibliography **26**

List of Figures

1 Jablonski Diagram 2
2 Fluorescence signal generation and collection 3
3 Parameter space of fluorescence microscopy of live biological samples 4
4 Fluorescence light-sheet microscopy 5
5 Methods to generate light-sheet 5
6 Intensity distribution of the image of a point light source 6
7 Ventral furrow formation in *Drosophila* 8
8 Subpopulations of cells along DV axis 8
9 Imaging Volume 9
10 Strategies for improving deep-tissue imaging 11
11 Image processing pipeline for multiview deconvolution 18
12 Comparison of membrane markers 19
13 Embryo expressing GAP43::iRFP670 as membrane marker 20
14 Surface view of embryo expressing GAP43::iRFP670 as membrane marker 20
15 Fused and deconvolved images of cross-sections of embryo expressing GAP43::mCherry as membrane marker 21
16 Fused and deconvolved images of cross-sections of embryo expressing GAP43::mCardinal as membrane marker 22
17 ROIs for comparison of signal-to-noise ratio between fused and deconvolved image 22
18 Signal-to-noise ratio at different depths in fused and deconvolved image 23

List of Tables

1 Characteristics of Fluorophores 12
2 Primers used for PCRs 15
3 Illumination laser and Detection filters used for imaging 16

ACKNOWLEDGEMENTS

I would firstly like to thanks my supervisor, Prof. Maria Leptin, for providing me with the opportunity to work with her research group at European Molecular Biology Laboratory, Heidelberg and explore the regime of the interaction of light with biological matter.

I would also like to acknowledge my thesis advisor, Dr Chaitanya Athale (Indian Institute of Science Education and Research, Pune) for his feedback and support during the project.

My sincere gratitude towards two most important persons - Sourabh and Catarina. Catarina introduced me to the molecular cloning and also played an important role in designing the transgenic constructs. Sourabh helped me in developing the thorough understanding of the project. He also introduced me with handing the fly embryos and different imaging protocols. I am also thankful to them for reading the thesis drafts and providing valuable suggestions. Both of them have been really supportive throughout the progress of work.

Special thanks to Tobias Rasse (ALMF, EMBL Heidelberg) for his enormous support in image processing. I would also like to thank Dimitri (Hufnagel group, EMBL Heidelberg) for introduction to SPIM and having lot of worthy discussions regarding optics involved in project.

I am also thankful to the other members of Leptin group - Sinja, Benedikt, Daniel, Eva, Juan, Julio, Alessandaro and Rok. Their valuable suggestions and feedbacks played an important role in the progress of my project. Also, because of them, I had a really nice time at EMBL Heidelberg.

Thanks to Sushmita Hegde (IISER Pune) for introducing me to the Drosophila as a model organism even before I came here.

And heartly thanks to my parents, brother and friends for supporting me and keep motivating me to forge ahead through the difficult phase. I would like to dedicate this thesis to my late grandfather.

THANKS!!

Introduction

Light is an important tool to retrieve the information about our universe. The development of light-based tools and advancements in the measurement of light has led to many scientific discoveries. Telescopes provided us with the better insight of outer space; microscopes played an essential role in the field of biology and medicine whereas modern spectral analysis laid the foundation of quantum mechanics which helps in understanding the nature of matter at sub-atomic scales.

The study and understanding of nature depend on the ability to visualise them or infer them through indirect measurements. The field of optics has played an essential role in providing a better insight of biological processes. The development of sophisticated microscopes has helped us in visualising the biological processes at different spatiotemporal scales which have a wide range of applications in the field of biology and medical sciences.

1.1 Fluorescence Microscopy

“The human eye requires contrast to perceive details of objects” [Kubitscheck, 2013]. Several methods have been developed to improve the contrast in microscopy which resulted in the wide range of application of optical microscopy in biology. Darkfield was the simplest method of improving the contrast in images, followed by the ideas of histochemical staining, phase contrast, and the contrast generated by differential interference of light were introduced. *Fluorescence* is one of the most popular contrasting technique which depends on the chemical compounds known as *fluorophores* or *fluorochromes*. It is the process of emission of photons by molecules to relax from higher energy state to their ground state which has been excited upon photo-illumination. The fluorophores absorb the light in a particular wavelength range and later re-emit the photons at higher wavelengths (Figure 1). The term '*fluorescence*' was first coined by G.G. Stokes in 1852 in his article *On the change of refrangibility of light*.

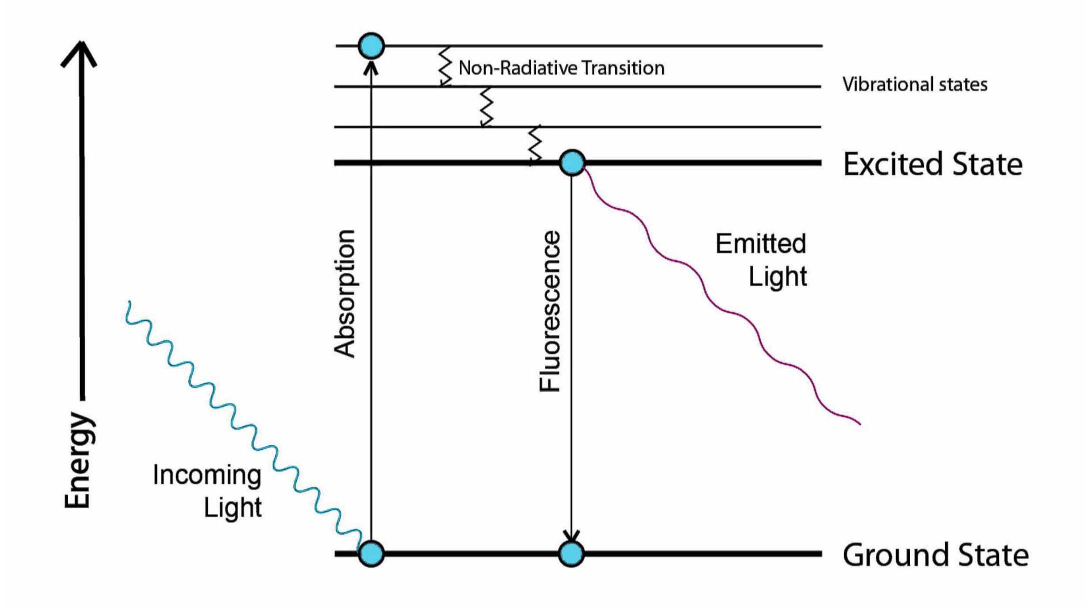

Figure 1: **Jablonski Diagram**: The molecules in the ground state can excite to the higher energy level by absorption of light energy (10^{-15} s). Molecules which gets excited to the lowest vibrational state of higher energy level relaxes spontaneously by emitting the absorbed photon. The molecules which contribute to fluorescence relaxes from upper vibrational states to lowest vibrational states by dissipating their energy in the form of heat and then relaxes to the ground state (10^{-9} s) (adapted from [Kubitscheck, 2013]).

The first fluorescence microscope was developed by Otto Heimstaedt and Heinrich Lehmann (1911-1913). Later the isolation of Green Fluorescent Protein (GFP) from *Aequorea victoria* by Osamu Shimomura [Shimomura et al., 1962] and the successful attempts in tagging the GFP to the protein of interests with GFP in the 1990s revolutionised the role of fluorescence microscopy in fundamental research. It offers the possibility to visualise different cells, their cellular components or even proteins of interest in the specimen, thus facilitating the observations of biological processes in live samples.

A range of cyan [Heim et al., 1994] and yellow [Orm et al., 1996] fluorescent proteins was developed by modifying the wild-type GFP protein matrix and mutations in chromophore-forming residues. Later, the discovery of GFP-like molecules emitting in the red part of the visible spectrum among corals facilitated the multi-colour imaging [Matz et al., 1999]. In the past few years, the discovery of fluorescent proteins emitting in the infrared region has paved a way towards deep-tissue single photon microscopy [Shu et al., 2009]. Such fluorophores which were initially discovered showed longer maturation rates and lower photostability than the ones in available in the visible spectrum, but the recent studies have tried to overcome these limitations by use of different bacterial phytochromes [Shcherbakova and Verkhusha, 2013].

1.1.1 Challenges in fluorescence microscopy

The notion of ideal fluorescence microscopy of live specimens can be referred to the fast acquisition of images with high spatial resolution and low photobleaching and phototoxicity. However, this ideal condition is limited by the diffractive nature of light, the sensitivity of live specimens to light, the photostability of fluorophores and imperfections in optical components.

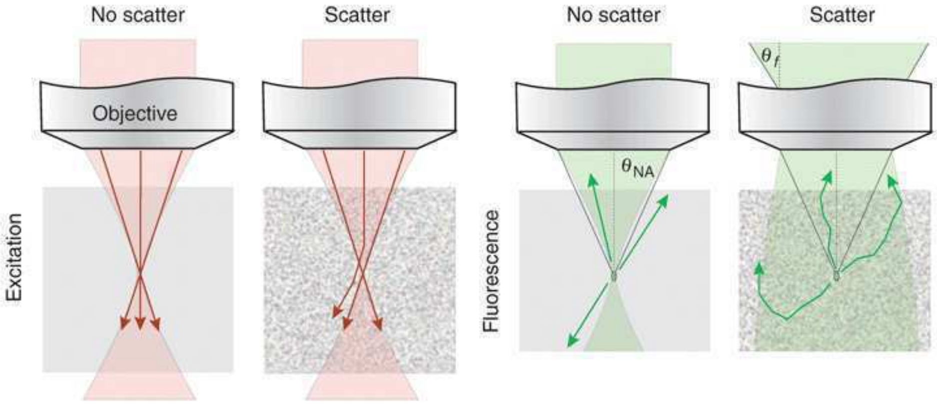

Figure 2: **Fluorescence signal generation and collection**: In a non-scattering tissue (No scatter); all the excitation light is focused onto the focal point of the objective. However, in a scattering tissue (Scatter), the excitation of the fluorophore decreases exponentially because of the deviation of the light as it propagates through the tissue. One needs to collect all the fluorescence signal generated in the focal plane of the objective. The light collection capability of an objective is determined by its numerical aperture (NA). In case of a non-scattering tissue, the signal generated in collection cone of the lens is detected. However, in a scattering tissue, the generated fluorescence signal encounters multiple deviations from its original path. Thus, the detected signal is collected from a larger field of view, determined by the angular acceptance range (θ_f) of the objective, in case of a scattering tissue (adapted from [Helmchen and Denk, 2005]

.

While dealing with thick samples, the scattering and absorptive properties of biological tissues affect the signal-to-noise ratio at greater depths. Due to the presence of lipids, organelles and other scatterers in biological tissue, both the illumination light and emitted fluorescence signal is affected (Figure 2). The scattering and absorption of incident light reduce the efficient excitation of fluorophores in the focal plane. Thus, as we go image deeper into the tissue, the fluorophores are not efficiently excited because the intensity of excitation light reduces. Moreover, the absorption of these scattered photons in the regions other than imaging plane will result in increased noise in images. The fluorescence signal coming from the deeper planes inside the tissue will encounter the same fate and will be scattered which results in reduced contrast in images [Helmchen and Denk, 2005].

The four important imaging parameters – spatial and temporal resolution of the

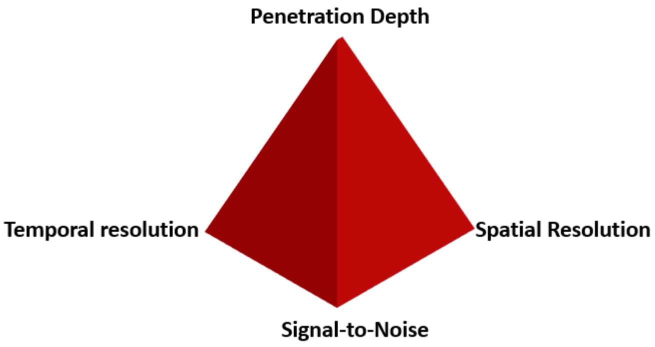

Figure 3: **Parameter space of fluorescence microscopy of live biological samples**: The balance between the four important imaging parameters, shown on the vertices of the tetrahedron, is required to be maintained for optimal imaging. Optimising one of the parameters reduces the maximum achievable performance of at least one of the other (adapted from [Keller, 2013])

.

optical microscope, penetration depth of light into the sample and signal-to-noise ratio in the microscopy images – are required to be maintained for optimal imaging [Keller, 2013]. However, optimising one of the parameters affects at least one of the others which pose a challenge to achieve the condition of ideal microscopy.

1.2 Selective Plane Illumination Microscopy

Selective Plane Illumination Microscopy (SPIM) is a fluorescence microscopy technique in which a thin light-sheet is used to illuminate the sample, and the fluorescence signal is collected along the orthogonal axis with respect to the illumination direction (Figure 4)[Huisken and Stainier 2009].

There are two ways in which a light-sheet can be created (Figure 5). A static light-sheet can be created by use of cylindrical optics whereas a digitally scanned light-sheet can be created by using galvanometric scanned mirrors to rapidly move a focused beam up and down [Kromm et al., 2016]. The fluorescence signal can be detected with the use of a charged coupled device (CCD) or scientific complementary metal-oxide semiconductor (sCMOS) cameras.

SPIM has become one of the important tools for studying development in complex model organisms such as zebrafish, medaka and *Drosophila*. SPIM is advantageous over conventional microscopy system as it offers reduced photobleaching and high-speed data acquisition [Krzic et al., 2012, de Medeiros et al., 2015]. These benefits make it suitable for extended time-lapse experiments. The possibility of recording the sample from different views and the reconstruction of this multiview acquisition serves

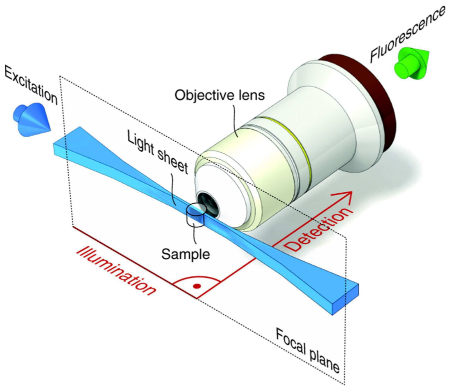
Fluorescence
Excitation
Objective lens
Light sheet
Sample
Detection
Illumination
Focal plane

Figure 4: **Fluorescence light-sheet microscopy**: Fluorescence excitation (blue arrow) and detection (green arrow) are decoupled into two orthogonal optical paths in light-sheet microscopy (adapted from [Huisken and Stainier 2009]).

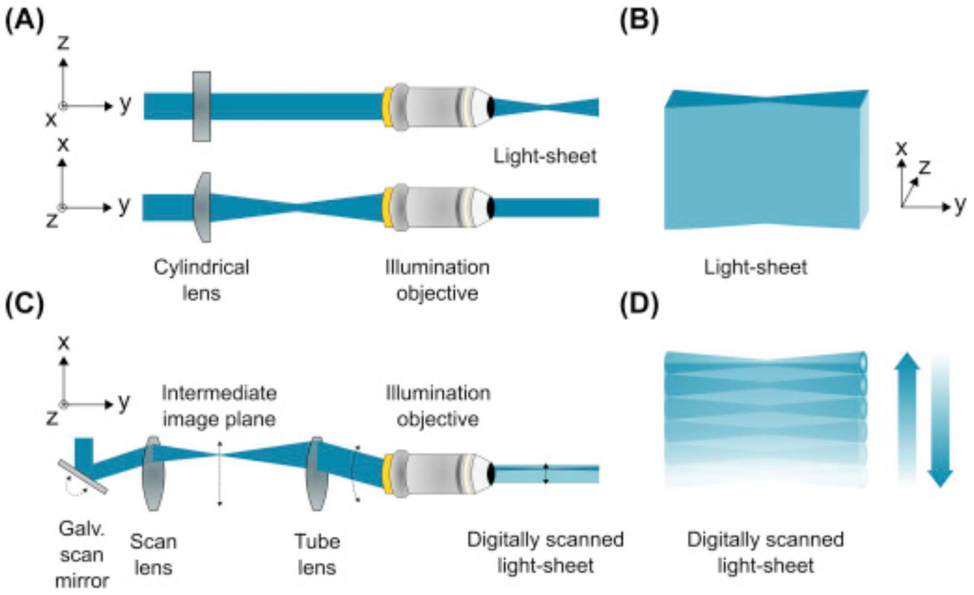
(A)
z
y
x
x
y
z
Light-sheet
Cylindrical lens
Illumination objective
(B)
x
z
y
Light-sheet
(C)
x
y
z
Intermediate image plane
Illumination objective
Galv. scan mirror
Scan lens
Tube lens
Digitally scanned light-sheet
(D)
Digitally scanned light-sheet

Figure 5: **Methods to generate light-sheet**: (A-B) Static light-sheet: With the use of cylindrical lens, the Gaussian beam is focused before it enters the illumination objective (xy-plane) which results in creation a light-sheet which is extended in xy-plane and focused along the z-axis. (C–D) Digitally scanned light-sheet: For creating a digitally scanned light-sheet, a combination of a galvanometric scan mirror, a scan lens and a tube lens is used instead of cylindrical lens. The galvanometric scan mirror is rotated which leads to translation of beam along x-axis in the intermediate image plane as it passes through the scan lens. Further, the combination of the tube lens and illumination objective creates a scanned light-sheet which translates along the x-direction (adapted from [Kromm et al., 2016]).

an important purpose in *in toto* study of optically opaque samples such as *Drosophila* embryos [Krzic et al., 2012, de Medeiros et al., 2015].

1.3 Deconvolution in Optical Microscopy

The blurring in the light microscopy images is partially random, but it mainly results due to the diffraction of light as it passes through the optical components and apertures, the scattering of light from the sample and refractive index mismatch in the path of light [Cannell et al., 2006]. All these factors affect the correspondence between the source of light and its final location in the image plane.

Mathematically, the image (i) formation using an optical microscope can be described as the convolution ($\otimes$) of the object (o) and the point spread function (psf) of the optical system (1.1)[Kubitscheck, 2013].

$$i(\overrightarrow{\mathrm{r}}) = o(\overrightarrow{\mathrm{r}}) \otimes psf(\overrightarrow{\mathrm{r}}) \tag{1.1}$$

The PSF of an optical system is the multi-dimensional image of a point in space (Figure 6). The point source emits light radially (w_0) which is transformed by the objective lens into a parallel wave. According to Huygens principle, the wavefronts of the parallel wave serves as a source of secondary wavelets. A tube lens is then used to project the light onto the image plane. The image formed depends on the interference of a finite range of wavelets collected by the tube lens which results in image as a smeared spot (Figure 6). One can measure the PSF of an optical system by imaging the diffraction-limited beads or can compute it theoretically based on the optical parameters-such as the numerical aperture of the objective, beam diameter etc. - of the system [Kubitscheck, 2013].

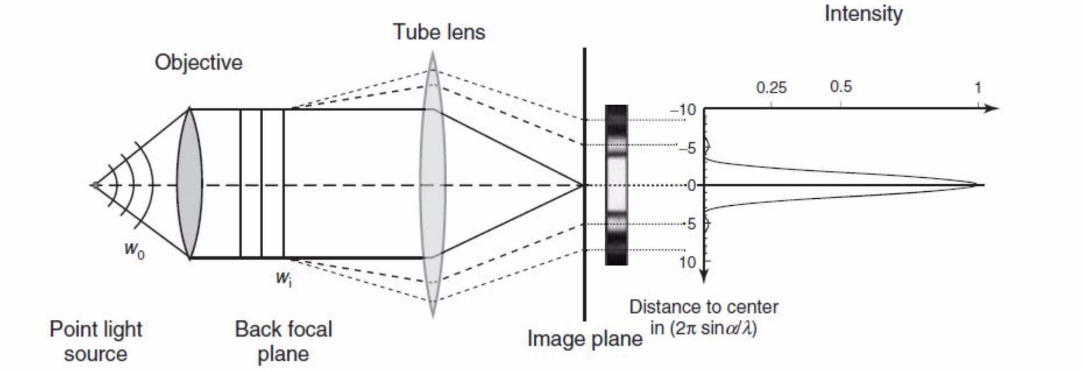

Figure 6: **Intensity distribution of the image of a point light source**: The image is a result of interference of wavelets originating from the exit pupil of the objective lens. The image of the point light source, formed by the system, is its Point Spread Function (PSF). The wavelets originating from wavefront w_i in the back focal plane of objective (plane passing through the rear focal point of lens and orthogonal to principle optic axis) are collected by the tube lens after which they undergo interference to give a smeared spot as image of the point source (adapted from [Kubitscheck, 2013]).

Deconvolution is the reverse operation which helps in obtaining the original object from the microscopy images. The contribution of out-of-focus fluorescence from the image plane is removed which results in improving the contrast in the image. It also (partially) reverses aberrations arising from imperfections in the optical arrangements [Cannell et al., 2006]. The knowledge of accurate PSF of the system is important for improving the deconvolution. The image restoration can also be improved firstly by oversampling the data while acquisition and secondly by minimising the effects of CCD defects (dead pixels) [Sibarita, 2005, Chung et al., 2012]. According to the Nyquist theorem, the sampling distance should be half of the PSF [Sibarita, 2005]. While reconstructing the original object, deconvolution algorithms guess the information of the high-frequency components which were not recorded. Oversampling minimizes the artefacts arising due to this guess.

1.4 Ventral furrow formation in *Drosophila melanogaster*

Drosophila embryogenesis has been an attractive model to study the role of cell shape changes in large-scale morphogenetic events. The early stages (stages 5-11) of development in Drosophila embryo include three morphogenetic events – tissue internalisation, convergence and extension of main body axis and segmentation [Lye and Sanson, 2011]. Early blastoderm consists of a monolayer of epithelial cells which has an apical-basal polarity with apical side facing outside and basal inside. These cells are indistinguishable from each other just before the onset of gastrulation (except the pole cells). Ventral furrow formation (VFF) (Figure 7) is the first large-scale morphogenetic event in fly embryo. During this event, the presumptive mesodermal cells on the ventral side of embryo form a furrow and get internalised [Leptin and Grunewald, 1990].

During the VFF, the cells along the dorsoventral (DV) axis can be divided into four subpopulations based on their movements and apical surface area changes (Figure 8) [Leptin and Grunewald, 1990, Rauzi et al., 2015]. The cells along the ventral midline of embryo form the future mesoderm. These mesodermal precursor cells consist of two subpopulations. The central mesodermal (CM) cells (8-10 cells) constrict apically. Their immediate neighbours, lateral mesodermal (LM) cells (3-4 cells wide on each side of CM cells), shows expansion of the apical surface (red cells in Figure 8). The lateral cells retain their shape and move as a group towards the ventral midline in response to the invagination of furrow whereas the dorsal cells stretch along the DV axis.

Drosophila Folded gastrulation (Fog) pathway is a key regulator of the

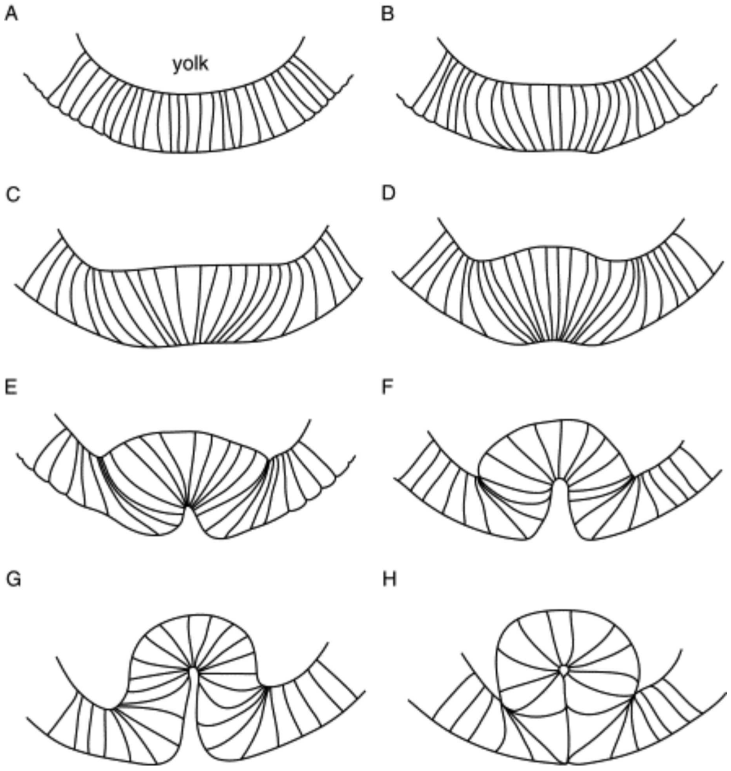

Figure 7: **Ventral furrow formation in *Drosophila***: The sections show the ventral part of the embryo, with the apical side of the cells facing outside (bottom) and the basal side contacting the yolk (top). (A) The ventral-most cells (presumptive mesoderm) have flattened apically and mild apical constriction can be noted in some cells. (B–D) Further apical constriction occurs in the most ventrally situated cells, while the slightly more lateral apically flattened cells expand their apices. The ventral cells elongate in the apicobasal axis, and a shallow groove is formed. (E and F) The apically constricted cells shorten in length as invagination occurs (and the ventral furrow forms). (G) Invagination completes resulting in the complete internalisation of the mesodermal cells through the ventral furrow. (H) The ventral furrow closes leaving a tube of mesodermal cells that remain attached to the ectoderm (adapted from [Lye and Sanson, 2011]).

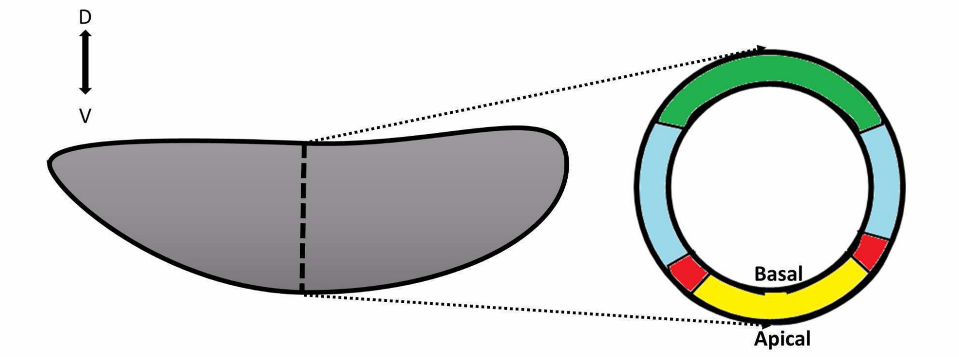

Figure 8: **Subpopulations of cells along DV axis**: The cells along the DV axis can be divided into four subpopulations - Central mesodermal cells (yellow), lateral mesodermal cells (red), lateral cells (cyan) and dorsal cells (green)- on the basis of their cell shape changes during VFF.

cell shape changes blastodermal epithelium ([Dawes-Hoang et al., 2005, Manning and Rogers, 2014]). The two transcription factors, *twist (twi)* and *snail(sna)*, initiate and control the shape changes in the ventral cells [Leptin, 2005, Martin et al., 2009]. It is through the action of their downstream targets; an apical supracellular actomyosin meshwork is recruited in the CM cells. This actomyosin meshwork contracts and causes constriction of the apical side of the CM cells. It has been well-documented that highly coordinated constriction of apical surface of the CM cells drives the furrow formation [Martin et al., 2009]. LM cells also express the mesodermal differentiation factors *twi* and *sna* but are not invaginated and form the stalk of the furrow.

In *Drosophila*, the two subpopulations (CM and LM cells) show different shape changes during VF formation even though they show the same expression of mesodermal transcription factors - *sna* and *twi* [Leptin and Grunewald, 1990, Leptin, 1991]. In the previous studies on VF formation, we observed in the cross-sections of fixed embryos that basal area reduces in the LM cells [Leptin and Grunewald, 1990, Leptin and Roth, 1994, Fuse et al., 2013]. However, the role of LM cells in the invagination of furrow remains unclear mainly because of the limitations in imaging their complete volume and rapid shape changes at high spatiotemporal resolution.

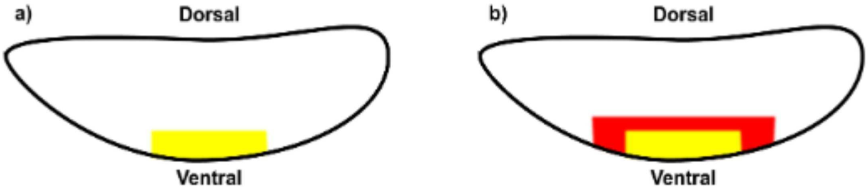

Figure 9: **Difference in imaging volume to study the cell shape changes during VFF**: (a) Recording CM cells only (yellow) (b)Additional volume required to be imaged (red) for recording the shape changes in LM and CM cells

Two-photon excitation based confocal microscopes have proven to be essential tools in resolving the cellular dynamics deep inside the embryos during the early stages of development in *Drosophila* [Gelbart et al., 2012]. The LM cells are the first subpopulation along DV axis that responds to shape changes in CM cells [Rauzi et al., 2015]. Thus, to understand dynamics of LM cells, they have to be investigated along with the CM cells. However, using two-photon excitation microscopes, recording the complete volume of LM cells along with CM cells makes it difficult to capture the fast shape changes of LM cells (Figure 9). Previous studies show that

SPIM can also achieve similar imaging depths as two-photon excitation microscopes [Pediredla et al., 2016]. Besides this, the advantages of low-phototoxicity and high-speed data acquisition makes it suitable for embryo-scale cellular and tissue dynamics [Keller, 2013, Rauzi et al., 2015].

Scope and delimitations

This study aims at improving the single photon deep-tissue imaging using the selective illumination microscope in *Drosophila* embryos. The depth of imaging is mainly limited by the scattering of light. Further, the presence of blur in the images affects the quantitative analysis of cell shape changes. The main objectives are:

- improve the signal to noise ratio as we image deeper in the tissue.
- computationally reduce the noise and blur in microscopy images

We developed transgenic fly lines with each line expressing a different fluorescent protein tagged membrane markers. The cloning of GAP43::iRFP682 and GAP43::iRFP702 constructs took additional time in comparison to the GAP43::mCardinal and GAP43::iRFP670. In this study, due to the time constraints imposed by the cloning of the transgenic constructs and later generation of fly stocks, we only compared the expression of GAP43::mCardinal and GAP43::iRFP670 in heterozygous fly stocks.

Materials and Methods

2.1 Methodology

Our approaches to improve the deep-tissue imaging using SPIM are summarised in Figure 10.

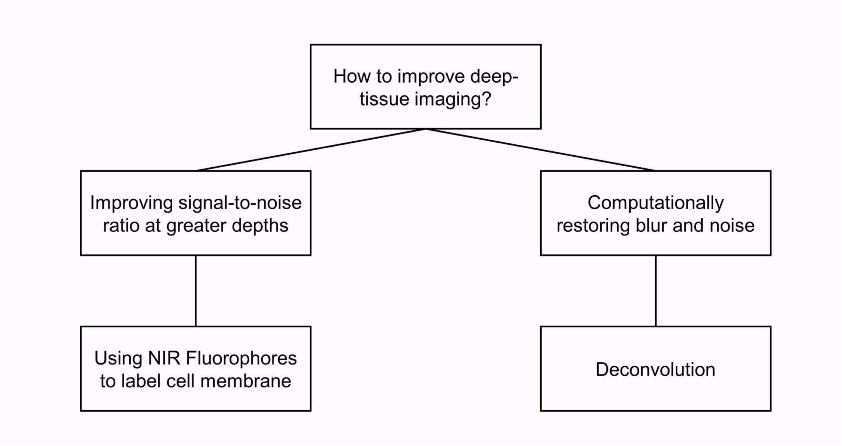
How to improve deep-tissue imaging?
Improving signal-to-noise ratio at greater depths
Computationally restoring blur and noise
Using NIR Fluorophores to label cell membrane
Deconvolution

Figure 10: **Strategies for improving deep-tissue imaging**: We will take a two way approach to improve deep-tissue imaging using SPIM - by developing new membrane markers to improve signal-to-noise ratio at greater depths and by using multiview deconvolution to reduce noise and blur present in raw images.

Improving the signal-to-noise ratio in microscopy images at greater depths

The scattering of light depends on its wavelength and the size of the scattering object [Strutt, 1871]. With the increase in wavelength, the scattering coefficient reduces which signifies that the scattering reduces. In any biological tissue, the fluorescence signal from the greater depths is affected by the scattering and absorption of light in the tissue [Jacques et al., 2013]. Thus, to increase the depth of imaging, we will use fluorophores emitting in the far-red and near-infrared region to develop new membrane markers.

Computationally restoring blur and noise

The presence of random noise and blur reduces the contrast in the light microscopy images. We will use multiview deconvolution to reduce the blur present in the SPIM images.

2.2 Generation of transgenic fly stocks

Fly lines expressing the protein that label the cell membranes were generated. The protein was tagged with the fluorophores emitting in the far-red and near-infrared region of the electromagnetic spectrum. We selected four fluorophores - mCardinal, iRFP670, iRFP682 and iRFP702 -based on their high quantum yield and photostability among the available far-red and near-infrared fluorophores [Chu et al., 2014, Shcherbakova and Verkhusha, 2013].

Flurophore	Excitation maxima(nm)	Emission maxima(nm)	Quantum Yield($\%$)	Photostability (s)
mCardinal	604	658	19.0	730
iRFP670	642	670	12.2	290
iRFP682	663	682	11.1	490
iRFP702	673	702	8.1	630

Table 1: Characteristics of Fluorophores

These fluorophores were tested for deep-tissue imaging in the mammalian tissues [Chu et al., 2014, Shcherbakova and Verkhusha, 2013]. Since none of these fluorophores was previously expressed in flies, we develop new transgenic constructs. A fragment of the GAP43 protein (from *Bos taurus*) tagged with the fluorophores was cloned. This fragment corresponds to first 20 amino acids of GAP43 protein which binds to the lipids present in the plasma membrane and thus marking at the membranes with the fluorophores [Mavrakis et al., 2009, Zacharias et al., 2002].

To promote high expression of the fluorophore (iRFP) tagged GAP43, this protein was cloned downstream of the tubulin promoter. Tubulin is a protein which is expressed in microtubules (a major component of the eukaryotic cytoskeleton). This protein is highly expressed during the early stages of embryogenesis and using this promoter will induce high expression of the downstream gene GAP43:iRFP in the early embryos [Raff et al., 1982]. The *mini-white* gene was used as a selectable marker for transformation. A *K10* terminator was used as it helps in early transfer of RNAs from the nurse cells into oocytes and maximising the expression of the fluorophore-tagged GAP43 [Serano et al., 1994].

The constructs were inserted in the fly genome through the PhiC31- integrase-mediated transgenesis system [Bischof et al., 2007]. This is a genomic integration method which is based on site-specific $\phi C31$ integrase mediated integration between bacterial attachment site (attB) and phage attachment site (attP), present in the injected plasmid and fly genome respectively [Bischof et al., 2007]. This method is beneficial for the site-specific insertions of transgenes.

2.2.1 Plasmid Construction

The *attb-tubulin_promoter-K10* plasmid was constructed using *pCasper4-tubulin* (provided by Dr Stefano De Renzis, EMBL Heidelberg) and attb-UASp-K10 plasmid (provided by Dr Anne Ephrussi, EMBL Heidelberg). The *attb-UASp-K10* plasmid contains mini-white gene and terminator sequence from K10 gene. The *tubulin_promoter* sequence was amplified from the *pCasper4-tubulin* using the forward primer containing *StuI* site and the reverse primer containing *NotI* site. The amplified product was purified and digested with *StuI* and *NotI*. The *attb-UASp-K10* plasmid was also digested with StuI and NotI to remove the UAS promoter. The *tubulin_promoter* was then ligated to digested *attB-UASp-K10* plasmid to produce *attb-tubulin_promoter-K10* plasmid. The ligated plasmid was confirmed with diagnostic restriction digestion using EcoRV and Sanger sequencing.

The first 20 amino acids of GAP43 protein (from *Bos taurus*) was introduced into the forward primers for all the four fluorophores.

GAP43::mCardinal was constructed using the forward primer containing NotI site (underlined) and the reverse primer BamHI site (underlined) (Table 2) using the plasmid *mCardinal-H2B-C-1032* as a template (deposited by Dr Michael Davidson (Addgene plasmid #56162)).

GAP43::iRFP670 was constructed using the forward primer containing NotI site (underlined) and the reverse primer BamHI site (underlined) (Table 2) using the plasmid *pNLS-iRFP670* as a template (deposited by Dr Vladislav Verkhusha (Addgene plasmid #45466)).

GAP43::iRFP702 was constructed using the forward primer containing NotI site (underlined) and the reverse primer with BamHI site (underlined) (Table 2) using the plasmid *pBAD-HisB-iRFP702* as a template (deposited by Dr Vladislav Verkhusha

(Addgene plasmid #45455)).

All the GAP43::iRFPs constructs were purified and digested with *NotI* and *BamHI*. Each PCR product was ligated to similarly digested *attb-tubulin_promoter-K10* plasmid to produce *attb-tubulin_promoter-GAP43::mCardinal-K10*,*attb-tubulin_promoter-GAP43::iRFP670-K10* and *attb-tubulin_promoter-GAP43::iRFP702-K10* plasmids, respectively. These plasmids were then confirmed by diagnostic restriction digestion using *NcoI* and by Sanger sequencing.

GAP43::iRFP682 was constructed using the forward primer containing NotI site (underlined) and the reverse primer with XbaI site (underlined) (Table 2) using the plasmid *pBAD-HisB-iRFP68237* as a template (deposited by Dr Vladislav Verkhusha (Addgene plasmid #45454)). Due to the presence of *BamHI* restriction site in iRFP682 sequence, we introduce *XbaI* site in the reverse primer (also present in *attb-tubulin_promoter-K10* plasmid). The GAP43::iRFP682 construct was purified and digested with NotI and XbaI and then ligated to similarly digested *attb-tubulin_promoter-K10* plasmid to produce *attb-tubulin_promoter-GAP43::iRFP682-K10* plasmid. The plasmid was confirmed with diagnostic restriction digest using *NcoI* and by Sanger sequencing.

2.2.2 Fly transformation and Stock generation

0.27-0.38 $\mu g/\mu l$ of the *attb-tubulin_promoter-GAP43::iRFP-K10* plasmids with mCardinal, iRFP670 and iRFP702 were sent to the BestGene Inc. (California, USA) for injections into the embryos of flies with landing sites VK18 (#BDSC-9736) and VK33(#BDSC-9750) on II and III chromosomes respectively. All the ecloded adults (G0) were crossed with yw flies. The positive G1 transformants (red or orange eyes) were selected and were crossed with yw flies. The positive G2 males (red or orange eyes) were selected and crossed to II, and III chromosome balancers fly respectively.

The cloning of *attb-tubulin_promoter-GAP43::iRFP682-K10* plasmid required several troubleshooting. It was successfully cloned three weeks after the first batch of plasmids were sent to BestGene for injection. To avoid further delays, the plasmid was sent to Drosophila Injection service at EMBL, Heidelberg. 0.15 $\mu g/\mu l$ of the *attb-tubulin_promoter-GAP43::iRFP682-K10* plasmid was sent to Drosophila Injection Service (EMBL, Heidelberg) for the injections into the embryos of flies with landing sites VK18 (#BDSC-9736) and VK33(#BDSC-9750) on II and III chromosomes respectively. All the ecloded adults (G0) were crossed with II chromosome and III chromosome balancers flies. The positive G1 transformants (red or orange eyes) were selected and

Fragment amplified	Forward Primer (5' → 3')	Reverse Primer (5' → 3')
tubulin_promoter	tcatctaggcctgaattcgatatcaagcttgcac	tcatctgcggccgcgtaccttcacgctgtgg
GAP43::mCardinal	aaatatgcggccgccaccatgctgtgctgtatgcgaagaaccaaacaggttgaaaaaaatgatgaggaccaaaagattatggtgagcaagggcgag	tcatctgcggccgcgtaccttcacgctgtgg
GAP43::iRFP670	aaatatgcggccgccaccatgctgtgctgtatgcgaagaaccaaacaggttgaaaaaaatgatgaggaccaaaagattatggcgcgtaaggtcgatc	tcacgcggatccttagcgttggtggtgggc
GAP43::iRFP702	aaatatgcggccgccaccatgctgtgctgtatgcgaagaaccaaacaggttgaaaaaaatgatgaggaccaaaagattatggcgcgtaaggtcgatc	tcacgcggatccttagcgttggtggtgggc
GAP43::iRFP682	aaatatgcggccgccaccatgctgtgctgtatgcgaagaaccaaacaggttgaaaaaaatgatgaggaccaaaagattatggcggaaggatccgtc	tcacgctctagatcactcttccatcacgccg

Table 2: Primers used for PCRs

were crossed again with balancers flies. The positive G2 males (red or orange eyes) were selected and crossed to II, and III chromosome balancers fly respectively.

2.3 Fly stocks

The following stocks were used for imaging: *P[UASp-GAP43-Venus]*^{10}*/TM3Sb* (#BDSC-30896); *sqh-GAP43::mCherry/CyO* (provided by Dr Stefano De Renzis, EMBL Heidelberg); *tubulin-GAP43:mCardinal/TM6B* (this study) and *tubulin-GAP43:iRFP670/TM6B* (this study).

2.4 Imaging Protocol

2.4.1 Sample Preparation

Fly embryos were collected on apple juice agar plate placed at the bottom of a cage with adult flies at 25°C. The embryos were covered with Halocarbon 27 oil (Sigma-Aldrich) for staging the early cellularising embryos. Embryos were then dechorionated using 50% sodium hypochlorite solution for 3-4 min and were later washed with water to remove any impurity over the surface of the embryo.

The embryo was mounted in a glass capillary with the solution of 1% Phytagel (with 20 mM $MgSO_4$ solution). The fluorescent beads (size: 200nm) were also mixed with the Phytagel before loading it into capillary.

2.4.2 SPIM Imaging

Imaging was performed using MuVi-SPIM [de Medeiros et al., 2015]. The sample was illuminated using Nikon 10x/ 0.3NA W objectives and detected using the Nikon 20x/ 1.0NA W objectives. An additional tube lens of 1.5x magnification resulted in effective pixel size of $0.19\mu m * 0.19\mu m$. The optical sections were recorded with a typical spacing of $0.3\mu m$.

The illumination laser and detection filters used for imaging the respective fluorophore is given in Table 3. For comparison of different fluorophores as membrane markers, the embryos were imaged from the ventral side. The camera exposure time for all the recordings was 50ms. All the detections were done in confocal mode with slit size 40. For multiview deconvolution, the complete embryo was successively recorded at two orthogonal orientations for each time point.

Fluorophore	Illumination Laser	Detection Filter
Venus	515nm	526-564 BP
mCherry	561nm	572 LP
mCardinal	642nm	656 LP
iRFP670	642nm	656 LP

Table 3: Illumination laser and Detection filters used for imaging

2.4.3 Image Processing

Softwares used

All the cross-sectional views of the fly embryos were generated using the Fiji software (https://fiji.sc/). The *BigStitcher* software was used for further image processing (https://imagej.net/BigStitcher).

Multiview Fusion and Deconvolution

Pre-processing

The dead pixels were removed, and background camera noise was subtracted from the raw images.

Registration of multi-view dataset

The pre-processed images were imported in the *BigStitcher* software. Following transformations were applied to the imported images:

- **Calibration**: specify the pixel size and voxel depth (X,Y,Z)
- **Translation**: an image(size: a*b*c pixels) was translated by t(x) = -0.5*a, t(y)= -0.5*b and t(z) = -0.5*c*Z/X in x, y and z directions repectively.
- **Affine transformation**: The left camera images were taken as reference and the images acquired with right camera were flipped horizontally (along x axis) using affine transformation matrix (-1,0,0,0; 0,1,0,0; 0,0,0,1,0) to make the registration faster.

After applying the transformation, the multi-view dataset (pre-processed images) were registered using beads (embedded in the mounting medium) [Preibisch et al., 2010]

Image Fusion

The registered images were fused together using *BigStitcher* software. These images will be referred as *Fused* images in the ”Results” and ”Discussion” sections.

Multiview Deconvolution

An average PSF was measured using the detected beads. This PSF was then used for the multiview deconvolution. The multi-view dataset was then simultaneously deconvolved and fused together to give *Deconvolved* images. We used *Efficient Bayesian* *optimisation* (less fast, more precise) iteration and the deconvolved image was produced after 15 iterations. Tikhonov regularisation was used and Tikhonov parameter was set to 0.005.

The method to fuse and deconvolve images are summarised in Figure 11.

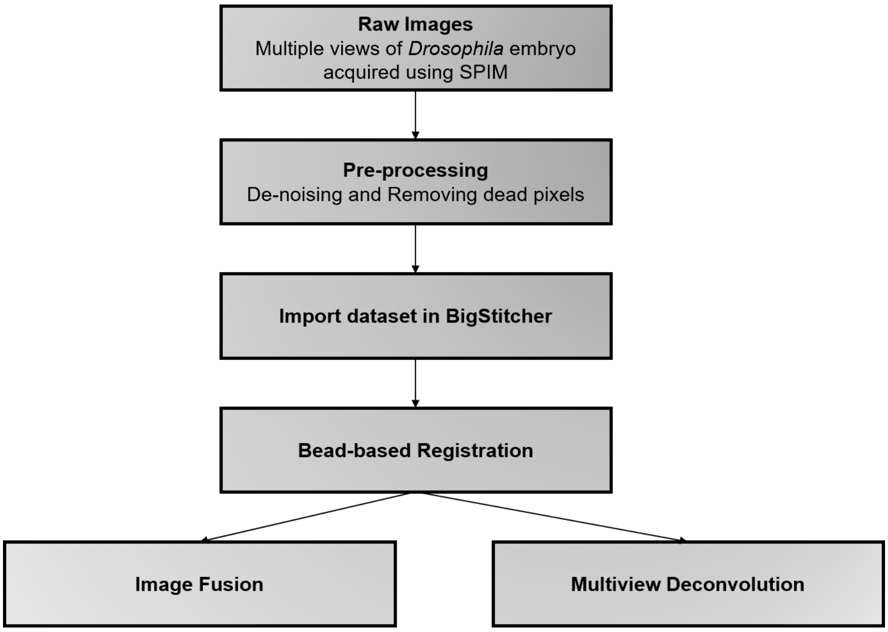
Raw Images
Multiple views of *Drosophila* embryo acquired using SPIM
Pre-processing
De-noising and Removing dead pixels
Import dataset in BigStitcher
Bead-based Registration
Image Fusion
Multiview Deconvolution

Figure 11: **Image processing pipeline for multiview deconvolution**: The raw images acquired using MuVi-SPIM. The images are pre-processed by removing dead pixels and subtracting background camera noise. The pre-processed images are then registered, fused and deconvolved using *BigStitcher* software

Multiview deconvolution is a memory intensive data processing technique. All the deconvolution were performed on EMBL HPC Cluster. Parallel cluster jobs for deconvolving all the time points were submitted which took 10-12 hours for deconvolving complete dataset for a single time point.

Data Analysis

Software used

The region of interests (ROI) were defined using FIJI software. The intensity measurements were done using FIJI software, and the graphs were plotted using OriginPro 9.

Intensity measurements

A fly embryo expressing GAP43::mCardinal as membrane marker was selected to compare the signal-to-noise ratio between the fused and deconvolved images. The intensity was measured for the ROIs at different depths for both the images.

Results

3.1 Comparison of different fluorophores as membrane markers

To improve the single-photon deep-tissue imaging in living Drosophila embryos, we developed transgenic flies with different fluorescent proteins – mCardinal, iRFP670, iRFP682 and iRFP702 – tagged to GAP43 as cell membrane markers.

For qualitative comparison between the new membrane markers with the existing ones, we recorded the development of embryos from cellularisation (Stage 5) till the invagination of ventral furrow. We compared mCardinal and iRFP670 with Venus and mCherry (Figure 12). Embryos were imaged from the ventral side using the MuVi-SPIM.

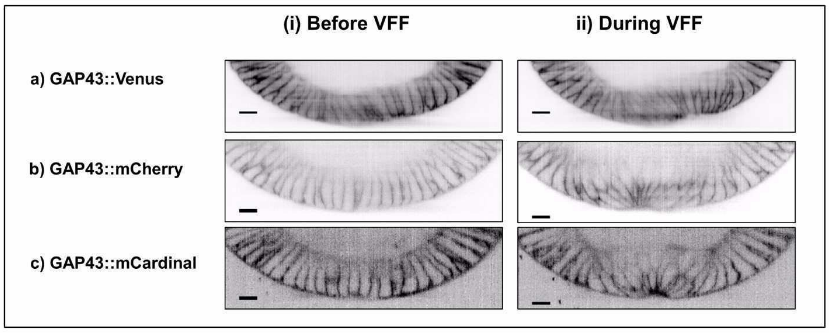

Figure 12: **Cross-sections of Drosophila embryos**: The cell membranes are labelled with different fluorophores-: a) GAP43::Venus, b) GAP43::mCherry and c) GAP43::mCardinal. The figure shows two different stages during Drosophila embryogenesis- i) Before and ii) During Ventral Furrow formation (VFF). The respective fluorophores are shown in black. Scale bar: $10 \mu m$

In case of GAP43::mCardinal, the interface of the basal end of epithelial cells and yolk is visible which signifies improved signal-to-noise ratio (Figure 12(c)). On the other hand, we observed very low fluorescence signal in case of GAP43::iRFP670 during the early stages of development (stages 5-6) (Figure 13). We then imaged an embryo for 12 hours at 30 min time interval to see if the fluorescence signal increases in the later stages or not. We observed an increase in fluorescence signal during the

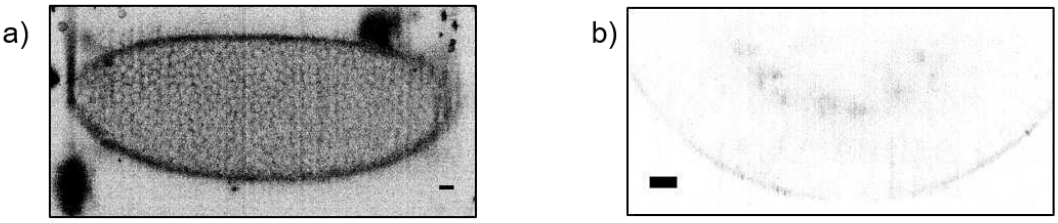

Figure 13: **Embryo expressing GAP43::iRFP670 as membrane marker**: a) Surface view and b) cross-section of Drosophila embryo. The cell membranes are labelled with GAP43::iRFP670 and shown in black. The LUT for surface view is adjusted to show the fluorescence signal in this figure. Scale bar: $10\mu m$

later developmental stages of embryos (Figure 14).

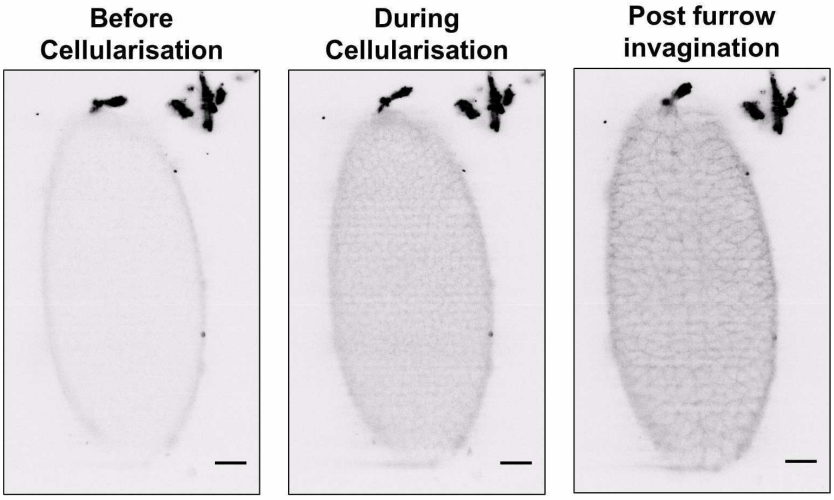
Before Cellularisation
During Cellularisation
Post furrow invagination

Figure 14: **Surface view of embryo expressing GAP43::iRFP670 as membrane marker**: The fluorescence signal increases after stage 6 (post invagination) in comparison to earlier stage (Before cellularisation) iRFP670 is shown in black (inside the embryo) Scale bar: $20\mu m$

3.2 Computationally restoring noise and blur using deconvolution

We used Multiview deconvolution to computationally reduce the noise and blur present in the SPIM images [Preibisch et al., 2014]. We imaged whole embryo with GAP43:mCherry and GAP43:mCardinal as membrane marker from two orientations using MuVi-SPIM. Before proceeding further with image fusion and multiview deconvolution, the images were pre-processed (Materials and Methods).

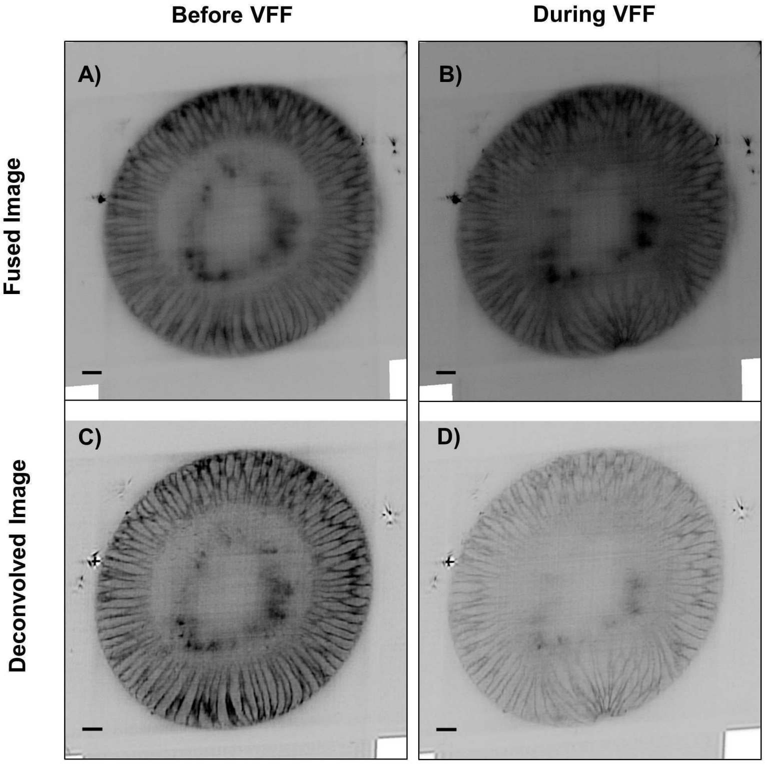

Figure 15: Fused and deconvolved images of cross-sections of embryo expressing GAP43::mCherry as membrane marker. Scale bar: $20\mu m$

We can observe an improvement in contrast in deconvolved images as the blur is reduced which improves the signal-to-noise ratio in images. We estimated the signal-to-noise ratio in the fused and deconvolved images by comparing the intensity along linear ROIs at different depths (Figure 17, 18). The intensity peaks corresponding to membrane are sharper in deconvolved image than in fused image at different depths, which signifies increase in signal-to-noise ratio in deconvolved images.

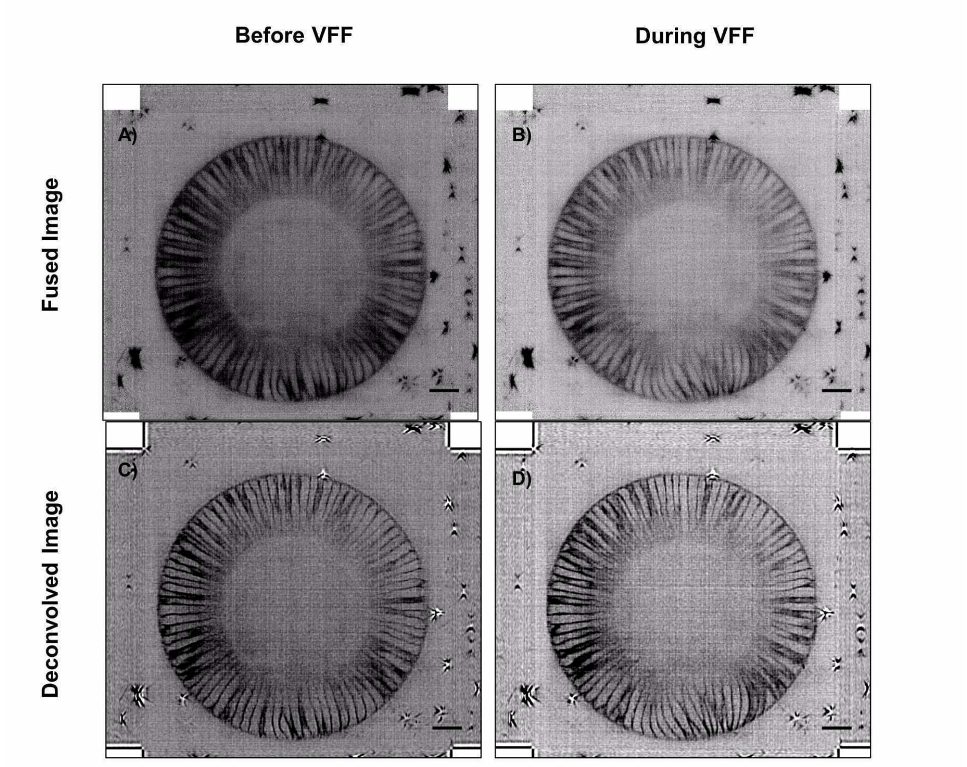
Before VFF
During VFF
Fused Image
Deconvolved Image
A)
B)
C)
D)

Figure 16: Fused and deconvolved images of cross-sections of embryo expressing GAP43::mCardinal as membrane markers. Scale bar: $20\mu m$

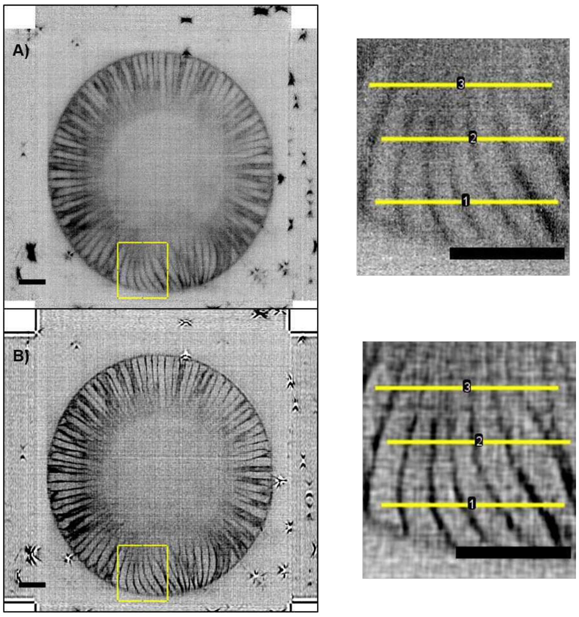

Figure 17: **ROIs for comparison of signal-to-noise ratio between fused and deconvolved image**: A) Fused image and B) Deconvolved image of cross-section of fly embryo expressing GAP43::mCardinal as membrane marker. The ROIs 1,2 and 3 are shown in the enlarged image of the insets. Scale bar: $20\mu m$

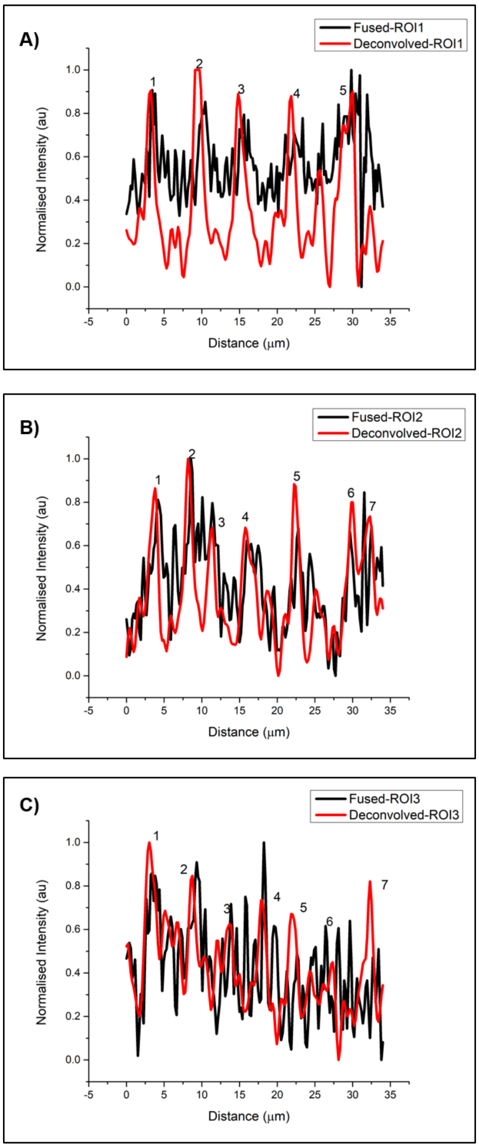

Figure 18: **Signal-to-noise ratio at different depths in fused and deconvolved image**: The intensity profile (black- Fused image; red - Deconvolved image) along the ROIs 1,2 and 3 (Figure 17) are shown in A, B and C respectively. The sharp peaks corresponding to membranes in deconvolved image are indexed.

Discussion

We developed fly stocks with new membrane markers with the far-red and near-infrared fluorophores – mCardinal, iRFP670, iRFP682 and iRFP702- tagged to GAP43 protein sequence. Amongst these membrane markers, we observed better signal-to-noise for GAP43::mCardinal when compared to that in GAP43::Venus and GAP43::mCherry. This observation is in agreement with the trends observed in previous studies of optical properties of biological tissue [Jacques et al., 2013]. Since mCardinal fluoresces at longer wavelengths, the fluorescence signal is scattered less and hence results in improved signal-to-noise ratio.

The embryos expressing GAP43::iRFP670 as membrane markers show low fluorescence signal at the early stages of embryonic development. One reason for low fluorescence could be the low availability of biliverdin. Infrared fluorophores are phytochrome based fluorescent proteins which recruit biliverdin as the chromophore to fluoresce [Shu et al., 2009]. Although, the fluorophores used in this study were shown to recruit the biliverdin present in the mammalian tissue for *in vivo* fluorescence and do not require biliverdin exogenously [Shcherbakova and Verkhusha, 2013]. In *Drosophila*, biliverdin is produced as the product of heme degradation [Cui et al., 2008]. It could be possible that during the early developmental stages, sufficient amount of biliverdin is not available for the maturation of chromophore. In the long-term recording (>10h) , we observed that the fluorescence increases at later stages. Therefore, we will inject biliverdin in early fly embryos and will observe the effect of exogenous biliverdin on fluorescence. Also, the remaining two new membrane markers, GAP43 tagged iRFP682 and iRFP702, will be tested soon.

We used multiview deconvolution to computationally reduce the noise and blur present in the fused images. Multiview deconvolution reduces the blur and enhances the membrane signal in the microscopy images. We observed shaper intensity peaks corresponding to membranes at different depths in case of deconvolved image than in fused image. To reduce the artefacts in image restoration, we filtered the dead pixels from the raw images. Also, we oversampled the data along z-direction by recording z-sections with spacing of 0.3 μm. However, the sampling density in the x and y directions is limited by the effective pixel size ($0.19\mu m * 0.19\mu m$). According to Nyquist theorem, the voxel size[1] for acquiring data using a 642nm laser on a MuVi-SPIM should be $0.163\mu m * 0.163\mu m * 0.305\mu m$. Thus, the availability of better pixel resolution will help in improving the deconvolution. The average PSF, computed from the detected fluorescent beads, is used as the input for the multiview deconvolution. A better estimate of PSF inside the embryo[2] will also help in improving the image restoration.

Images with high contrast are essential for performing the quantitative analyses of the cell shapes. The 3D reconstructions of LM cells during ventral furrow formation is limited by the low signal-to-noise ratio, especially towards the basal membrane . Now, we can obtain images with higher signal-to-noise ratio at greater depths with the new membrane marker GAP43::mCardinal which will facilitate in producing reliable 3D reconstructions of the cell shapes. These reconstructions will be helpful in the studying the cell shape changes in LM cells. The correlation of apical and basal surface area changes and quantitative analyses of volume of these cells during ventral furrow formation will be essential to determine whether these cells constrict basally or not [Gelbart et al., 2012].

---

[1] calculated using SVI NyquistCalculator (https://svi.nl/NyquistCalculator)

[2] This idea came out in discussion with Sourabh Bhide (Leptin group) and Dimitri Kromm (Hufnagel Group).

Bibliography

Bischof, J., Maeda, R., Hediger, M., Karch, F., and Basler, K. (2007). An optimized transgenesis system for Drosophila using germ-line-specific C31 integrases. Proceedings of the National Academy of Sciences, 104(9):3312–3317..

Cannell, M., McMorland, A., and Soeller, C. (2006). Image enhancement by deconvolution. pages 488–500. Springer US, Boston, MA.

Chu, J., Haynes, R. D., Corbel, S. Y., Li, P., Gonzalez-Gonzalez, E., Burg, J. S., Lin, M. Z., et al. (2014). Non-invasive intravital imaging of cellular differentiation with a bright red-excitable fluorescent protein. Nature Methods, 11(5):572–578.

Chung, J., Chung, M., and O'Leary, D. P. (2012). Optimal filters from calibration data for image deconvolution with data acquisition error. Journal of Mathematical Imaging and Vision, 44(3):366–374.

Cui, L., Yoshioka, Y., Suyari, O., Kohno, Y., Zhang, X., Adachi, Y., Ikehara, S., Yoshida, T., Yamaguchi, M., and Taketani, S. (2008). Relevant expression of drosophila heme oxygenase is necessary for the normal development of insect tissues. Biochemical and Biophysical Research Communications, 377(4):1156 –1161

Dawes-Hoang RE, Parmar KM, Christiansen AE, Phelps CB, Brand AH, Wieschaus EF. folded gastrulation, cell shape change and the control of myosin localization. Development. 2005 Sep;132(18):4165-4178

de Medeiros, G., Norlin, N., Gunther, S., Albert, M., Panavaite, L., Fiuza, U. M., Hufnagel, L., et al. (2015). Confocal multiview light-sheet microscopy. Nature Communications, 6(1):8881.

Fuse, N., Yu, F., and Hirose, S. (2013). Gprk2 adjusts Fog signaling to organize cell movements in Drosophila gastrulation. Development, 140(20):4246–4255.

Gelbart, M. A., He, B., Martin, A. C., Thiberge, S. Y., Wieschaus, E. F., and Kaschube, M. (2012). Volume conservation principle involved in cell lengthening and nucleus movement during tissue morphogenesis. Proceedings of the National Academy of Sciences of the United States of America, 109(47):19298–19303.

Heim, R., Prasher, D., and Tsien, R. (1994). Wavelength mutations and posttranslational autoxidation of green fluorescent protein. Proceedings of the National Academy of Sciences, 91(26):12501–12504.

Helmchen, F. and Denk, W. (2005). Deep tissue two-photon microscopy. Nature Methods, 2(12):932–940.

Hong, G., Antaris, A., and Dai, H. (2017). Near-infrared fluorophores for biomedical imaging. Nature Biomedical Engineering 1, 0010.

Huisken, J. and Stainier, D. Y. R. (2009). Selective plane illumination microscopy techniques in developmental biology. Development (Cambridge, England), 136(12), 1963–1975.

Jacques, S. (2013). Optical properties of biological tissues: a review. Physics In Medicine And Biology 58, R37-R61.

Keller, P. J. (2013). Imaging morphogenesis: Technological advances and biological insights. Science, 340(6137):1234168.

Kromm, D., Thumberger, T., and Wittbrodt, J. (2016). Chapter 5 - an eye on light-sheet microscopy. In Detrich, H. W., Westerfield, M., and Zon, L. I., editors, The Zebrafish, volume 133 of Methods in Cell Biology, pages 105 – 123. Academic Press

Krzic, U., Gunther, S., Saunders, T. E., Streichan, S. J., and Hufnagel, L. (2012). Multiview light-sheet microscope for rapid in toto imaging. Nature Methods, 9(7):730–733.

Kubitscheck, U. (2013). Fluorescence Microscopy: From Principles to Biological Applications, pages 23-128, Wiley-Blackwell.

Leptin M. (1991) *twist* and *snail* as positive and negative regulators during Drosophila mesoderm development. Genes Dev. 1991 Sep;5(9):1568-76.

Leptin, M. (2005). Gastrulation movements: The logic and the nuts and bolts. Developmental Cell, 8(3):305–320.

Leptin, M. and Grunewald, B. (1990). Cell shape changes during gastrulation in Drosophila. Development, 110(1):73–84.

Leptin, M. and Roth, S. (1994). Autonomy and non-autonomy in Drosophila mesoderm determination and morphogenesis. Development (Cambridge, England), 120(4):853–859.

Lye, C. M. and Sanson, B. (2011). Chapter five - tension and epithelial morphogenesis in drosophila early embryos. In Labouesse, M., editor, Forces and Tension in Development, volume 95 of Current Topics in Developmental Biology, pages 145 – 187. Academic Press

Manning, A. J. and Rogers, S. L. (2014). The Fog signaling pathway: Insights into signaling in morphogenesis. Developmental Biology, 394(1):6–14.

Martin, A. C., Kaschube, M., and Wieschaus, E. F. (2009). Pulsed contractions of an actin-myosin network drive apical constriction. Nature, 457(7228):495–499.

Matz, M. V., Fradkov, A. F., Labas, Y. A., Savitsky, A. P., Zaraisky, A. G., Markelov, M. L., and Lukyanov, S. A. (1999). Fluorescent proteins from nonbioluminescent Anthozoa species. Nature Biotechnology, 17(10):969–973.

Mavrakis, M., Rikhy, R., and Lippincott-Schwartz, J. (2009). Plasma membrane polarity and compartmentalization are established before cellularization in the fly embryo. Developmental Cell, 16(1):93–104

Orm, M., Cubitt, A. B., Kallio, K., Gross, L. A., Tsien, R. Y., and Remington, S. J. (1996). Crystal Structure of the Aequorea victoria Green Fluorescent.

Pediredla AK, Zhang S, Avants B, Ye F, Nagayama S, Chen Z, Kemere C, Robinson JT, Veeraraghavan A. Deep imaging in scattering media with selective plane illumination microscopy. J Biomed Opt. 2016 Dec 1;21(12):126009.

Preibisch, S., Amat, F., Stamataki, E., Sarov, M., Singer, R. H., Myers, E., and Tomancak, P. (2014). Efficient bayesian-based multiview deconvolution. Nature Methods, 11:645

Preibisch, S., Saalfeld, S., Schindelin, J., and Tomancak, P. (2010). Software for bead-based registration of selective plane illumination microscopy data. Nature Methods, 7:418

Raff, E. C., Fuller, M. T., Kaufman, T. C., Kemphues, K. J., Rudolph, J. E., and Raff, R. A. (1982). Regulation of tubulin gene expression during embryogenesis in drosophila melanogaster. Cell, 28(1):33 – 40

Rauzi, M., Krzic, U., Saunders, T. E., Krajnc, M., Ziherl, P., Hufnagel, L., and Leptin, M. (2015). Embryo-scale tissue mechanics during Drosophila gastrulation movements. Nature Communications, 6(1):8677.

Serano, T. L., Cheung, H. K., Frank, L. H., and Cohen, R. S. (1994). P element transformation vectors for studying Drosophila melanogaster oogenesis and early embryogenesis. Gene, 138(1-2):181–186.

Shcherbakova, D. M. and Verkhusha, V. V. (2013). Nearinfrared fluorescent proteins for multicolor in vivo imaging. Nature Methods, 10(8):751–754.

Shimomura, O., Johnson, F. H., and Saiga, Y. (1962). Extraction, purification and properties of aequorin, a bioluminescent protein from the luminous hydromedusan, Aequorea. Journal of Cellular and Comparative Physiology, 59(3):223–239.

Shu, X., Royant, A., Lin, M. Z., Aguilera, T. A., Lev-Ram, V., Steinbach, P. A., and Tsien, R. Y. (2009). Mammalian expression of infrared fluorescent proteins engineered from a bacterial phytochrome. Science, 324(5928):804–807.

Sibarita, J.- B. (2005) Deconvolution Microscopy. In: Rietdorf J. (eds) Microscopy Techniques. Advances in Biochemical Engineering, vol 95. Springer, Berlin, Heidelberg

Strutt, J. (1871). On the scattering of light by small particles. Philosophical Magazine, series 4, 41(275):447–454.

Swoger, J., Verveer, P., Greger, K., Huisken, J., and Stelzer, E. H. (2007). Multi-view image fusion improves resolution in three-dimensional microscopy. Opt. Express, 15(13):8029–8042.

Supatto, W., McMahon, A., Fraser, S. E., and Stathopoulos, A. (2009). Quantitative imaging of collective cell migration during Drosophila gastrulation: Multiphoton microscopy and computational analysis. Nature Protocols, 4(10):1397–1412.

Zacharias, D. A., Violin, J. D., Newton, A. C., and Tsien, R. Y. (2002). Partitioning of lipid-modified monomeric GFPs into membrane microdomains of live cells. Science, 296(5569):913–916

ADDENDUM

Title: Deep-tissue Imaging using Selective Plane Illumination Microscopy in *Drosophila*

Mayank Kumar

Results:

Comment by TAC: **Include negative results also.**

The results of cloning (plasmid construction) were not included in the thesis submitted earlier. The following section includes the results of cloning of *attB-tubulin_promoter-GAP43::iRFP plasmids* which include the negative results.

1. Plasmid Construction:

1.1 Construction of *attB-tubulin_promoter-K10* plasmid

The *attB-UASp-K10* plasmid, containing attB site and mini-white gene. To clone the GAP43::iRFP construct downstream of tubulin promoter, the UASp sequence was removed using restriction enzymes NotI and StuI. The larger fragment (V, Figure 1b.) with the attB site and the mini-white gene was then used as the vector backbone. The *tubulin promoter* (2632bp) sequence was amplified using *pCasper4-tubulin* plasmid as a template and ligated with the vector backbone extracted from the *attB-UASp-K10* plasmid. The ligated product was transformed using competent bacterial cells. We found seven bacterial colonies. The plasmid DNAs of all the colonies were tested using diagnostic restriction digest using NcoI (Figure 2.). All of the colonies gave the expected pattern which confirms the construction of *attB-tubulin_promoter-K10 plasmid*. The plasmid DNA extracted from colony 2 (lane 2 in Figure 2) was then sent for sequencing.

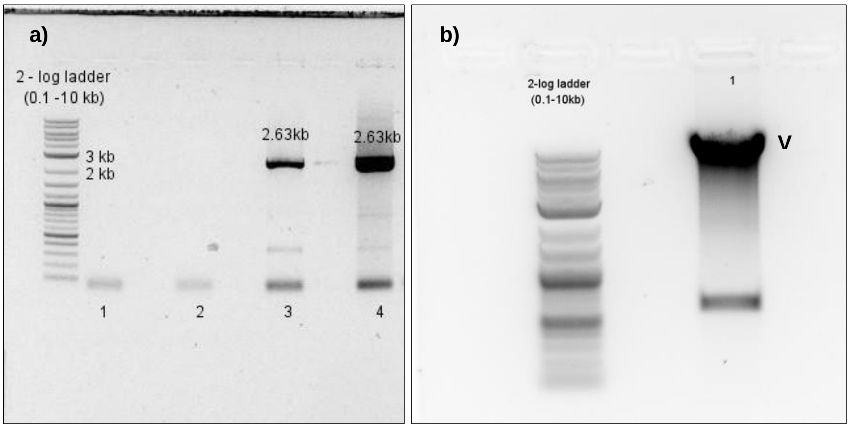

Figure 1: Construction of *attB-tubulin_promoter-K10* plasmid: a) PCR product of *pCasper4-tubulin.*The *tubulin promoter* (2.63kb, lane 3 and 4) were purified for further experiments. **b)** Restriction digest of *attB-UASp-K10* using StuI and NotI restriction enzymes. The band **V** was then purified to get the vector backbone with attB site and mini-white gene.

Initially, we obtained low concentration of the *tubulin promoter* after gel purification of PCR product of *pCasper4-tubulin*. We took another approach to extract the fragment with *tubulin promoter* from the *pCasper4-tubulin* plasmid. The plasmid was digested using AfeI and NotI restriction enzymes. The fragment with tubulin promoter (2.83 kb, Figure 3) was then ligated to the vector backbone extracted from the *attB-UASp-K10* plasmid. However, no colonies were found after the transformation.

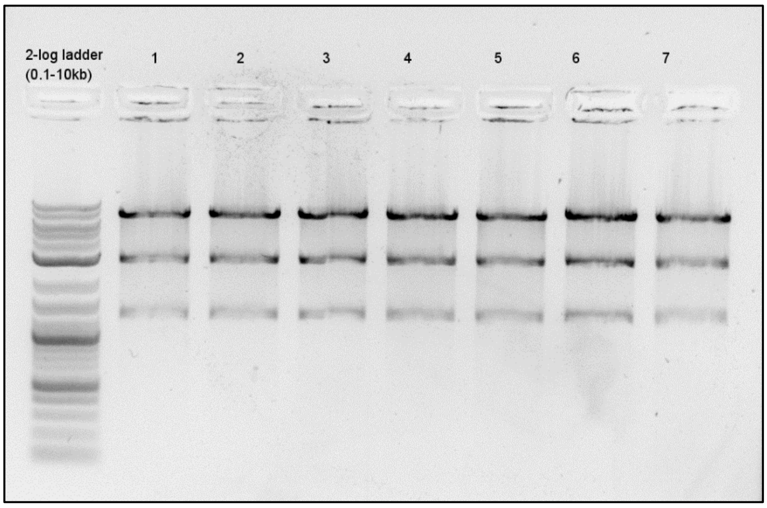

Figure 3: Diagnostic Restriction digest of *attB-tubulin_promoter-K10* plasmid using NcoI: The tubulin promoter (2632bp) was ligated to the vector backbone from *attB-UASp-K10*. After transformation, seven colonies were obtained, and the results of restriction digest using NcoI show that all the plasmids have tubulin promoter.

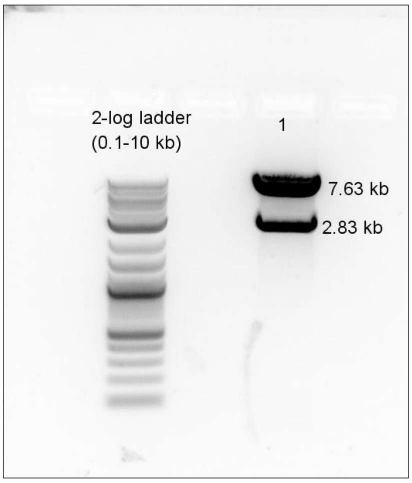

Figure 2: Restriction digestion of *pCasper4-tubulin*: *pCasper4-tubulin* plasmid was digested with restriction enzymes NotI and AfeI to amplify the fragment containing tubulin promoter (2.83 kb).

1.2 Construction of *attB-tubulin_promoter-GAP43::iRFP-K10* plasmids

For mCardinal, iRFP670, iRFP682 and iRFP702, the GAP43::iRFP constructs were amplified using forward and reverse primers containing NotI and BamHI sites, respectively (described in 2.2.1, Figure 4). These constructs were digested with enzymes NotI and BamHI and then ligated to similarly digested *attB-tubulin_promoter-K10* plasmid.

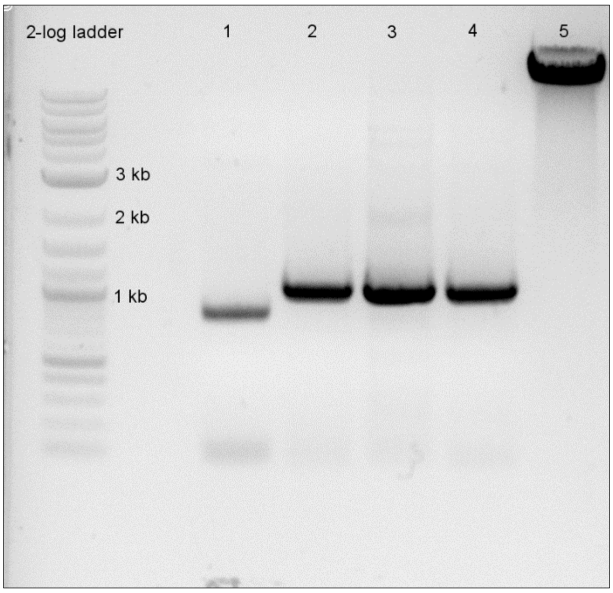

Figure 4: **Construction of attB-tubulin_promoter-GAP43::iRFP-K10 plasmids:** Lanes 1,2,3 and 4 shows the band corresponding to GAP43 tagged mCardinal, iRFP682, iRFP670 and iRFP702 respectively. The result of digestion of attB-tubullin_promoter-K10 using NotI and BamHI is shown in lane 5.

We obtained several bacterial colonies for mCardinal and iRFP670 after the first ligation. After changing the insert to vector ratio, we later got the transformed colonies for iRFP702. We tested plasmid DNAs from seven colonies each of mCardinal and iRFP670 and nine colonies using restriction digestion with NcoI (Figure 5). However, no positive colony was obtained in case of iRFP682. We later found out that it was due to the presence of BamHI restriction site in the iRFP682. Thus, we designed a new reverse primer with XbaI restriction site. The GAP43::iRFP682 fragment was then amplified using forward and reverse primer with NotI and XbaI respectively (Figure 6a). The fragment was digested using NotI and XbaI and then inserted in similarly digested *attB-tubullin_promoter-K10* plasmid (Figure 6b). Plasmid DNA from 12 bacterial colonies was tested using restriction digestion with NcoI (Figure 7).

The plasmid DNA from one colony of each of the fluorophores was then sent for sequencing to confirm the insertion of GAP43::iRFP constructs.

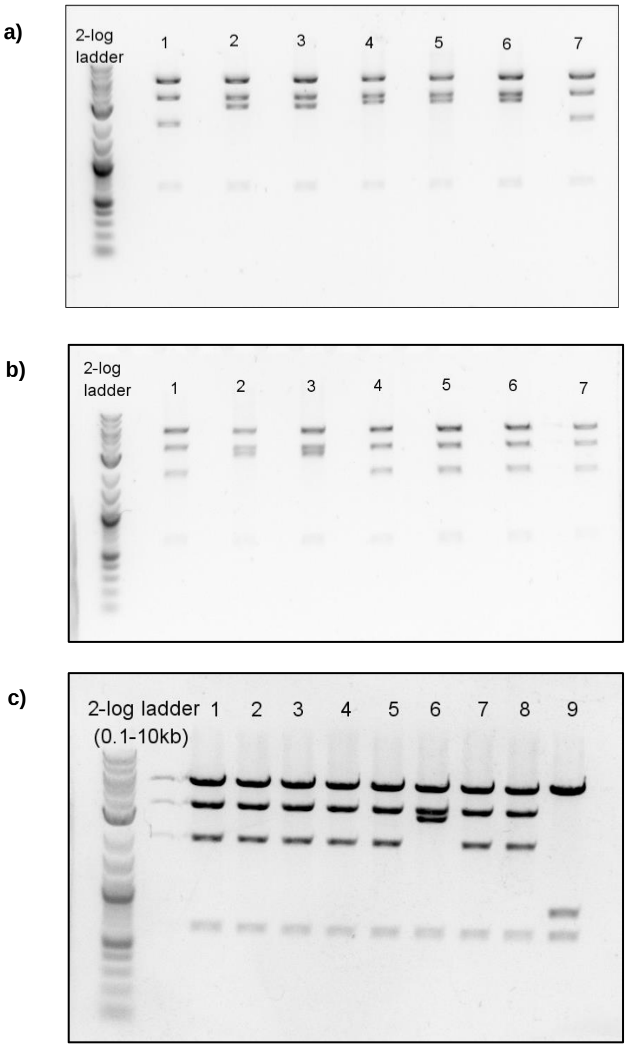
a)
2-log ladder
1
2
3
4
5
6
7
b)
2-log ladder
1
2
3
4
5
6
7
c)
2-log ladder
(0.1-10kb)
1
2
3
4
5
6
7
8
9

Figure 5: Diagnostic Restriction digest of *attB-tubulin_promoter-GAP43::iRFP-K10* plasmid using NcoI: a) mCardinal: Results of lanes 2,3,4,5 and 6 confirm the insertion of GAP43::mCardinal. **b) iRFP670:** Results of lanes 2 and 3 confirm the insertion of GAP43::iRFP670. **c) iRFP702:** Result of lane 6 confirms the insertion of GAP43::mCardinal.

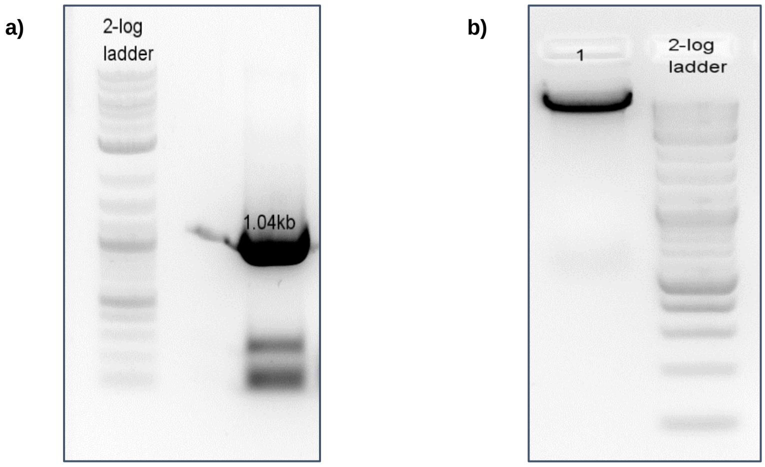
a)
2-log ladder
1.04kb
b)
1
2-log ladder

Figure 6: Construction of attB-tubulin_promoter-GAP43::iRFP682 plasmid: a) The fragment of GAP43::iRFP682 (1.04 kb) amplified using forward and reverse primer with NotI and XbaI sites.
b) The result of digestion of attB-tubullin_promoter-K10 using NotI and XbaI is shown.

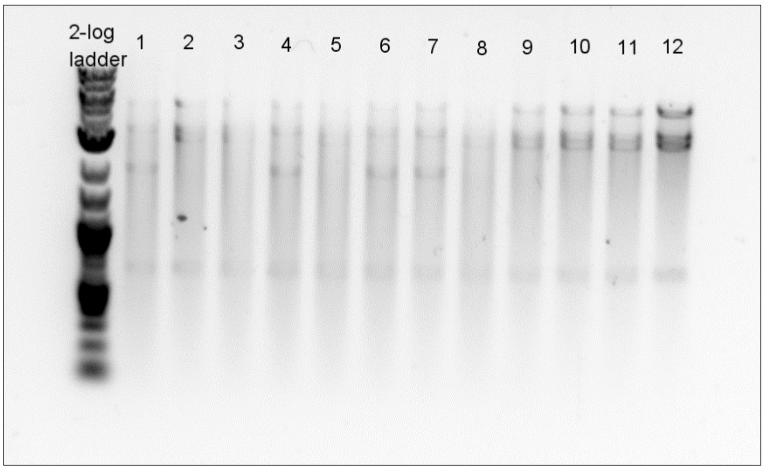
2-log ladder
1
2
3
4
5
6
7
8
9
10
11
12

Figure 7: Diagnostic Restriction digest of *attB-tubulin_promoter-GAP43::iRFP682-K10* plasmid using NcoI: Results of lanes 8,9,10,11 and 12 confirm the insertion of GAP43::iRFP682.

2. Computationally restoring noise and blur using deconvolution (Page 21-23)

Comment by TAC: Figure 17 and 18 can be combined and represented in the same figure to make the comparison more interpretable.

The combined figure, Figure 8, is shown below. The following figure will be indexed as Figure 17 in the thesis.

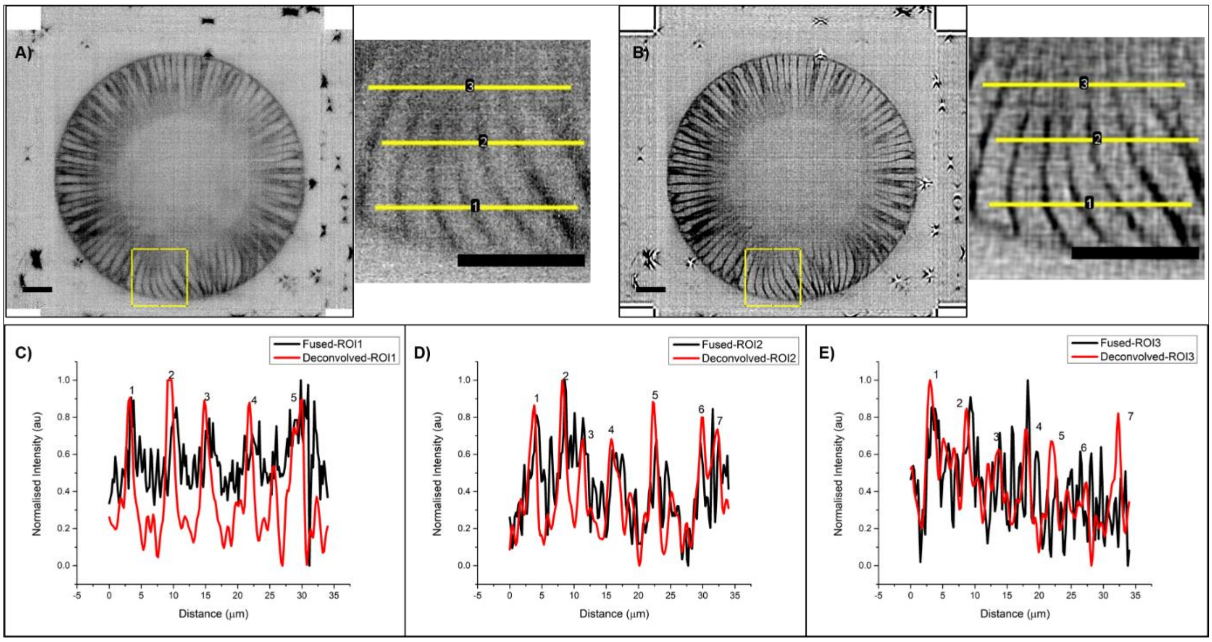

Figure 8 Signal-to-noise ratio at different depths in fused and deconvolved image: (A,B) The ROIs 1,2 and 3 are shown in the enlarged image of the insets. **(C,D,E)** Intensity profiles along the ROIs 1,2 and 3 are shown in C, D and E respectively. The sharp peaks corresponding to membranes in deconvolved image are indexed.

Deconvolution removes the blur present in the fused images which improve the signal-to-noise ratio. Therefore, we can observe an improvement in contrast in the deconvolved image in comparison with the fused images. We estimated the signal-to-noise ratio by comparing the intensity profiles at different depths in fused and deconvolved images. The intensity peaks corresponding to the membrane are sharper in the deconvolved image than in fused image which signifies the increase in signal-to-noise ratio in deconvolved image.